PRESSURE STRUCTURE OF SOLAR CORONAL LOOPS, III

T. D. SREEDHARAN*, K. SASIDHARAN, A. SATYA NARAYANAN,
and V. KRISHAN

Indian Institute of Astrophysics, Bangalore 560 034, India

Abstract. The theory of ideal magnetohydrodynamic turbulence in cylindrical geometry is used to study the steady-state structure of a coronal loop. The pressure profile is derived from MHD equations by representing the velocity and magnetic fields as the superposition of Chandrasekhar–Kendall functions. Such a representation brings out the three-dimensional structure of the pressure in the coronal loop. The radial, azimuthal, and axial variations of the pressure for a constant density loop are discussed in detail. The pressure has an oscillatory behavior for different azimuthal angles at some radial positions. This study predicts more features in pressure than can be compared with the presently available observations.

1. Introduction

It is well known that the solar corona is highly structured. The basic structural component of the solar corona is the coronal loop. These loops or arch-like structures of the active regions of the Sun have been observed in the emission at the UV, FUV, and X-ray wavelengths (Foukal, 1978; Levine and Withbroe, 1977; Vaiana and Rosner, 1978) The theory of radio pulsations in coronal loops has been discussed by Aschwanden (1987).

Coronal loop plasma is believed to carry currents which result in a helical form of the magnetic field (Levine and Altschuler, 1974; Poletto *et al.*, 1975; Krieger, de Feiter, and Vaiana, 1976; Priest, 1978, Hood and Priest, 1979). The MHD equilibria of coronal loops have been investigated by Priest (1981) and Tsinganos (1982).

In spite of the continuous pumping of magnetic and velocity field fluctuations into the coronal plasma, the loops exhibit a fairly stable and well configured geometry. The steady-state pressure structure is the result of the various manifestations of the balance of the inertial and magnetic forces. Krishan (1983a, b) discussed a steady-state model of active region coronal loops using the statistical theory of incompressible magneto-hydrodynamic turbulence described by Montgomery, Turner, and Vahala (1978). The main features of the theory consists of using the MHD equations for an incompressible fluid. The magnetic and velocity fields are expanded in terms of Chandrasekhar–Kendall (hereafter referred to as C–K) functions for which, the completeness has been proved by Yoshida and Giga (1990). The pressure profile is derived as a function of the velocity and magnetic fields in the form of Poisson equation. The spatial profiles of lines in active region loops were also studied. The statistical mechanics of velocity and magnetic fields in solar active regions was discussed by Krishan (1985). Krishan, Berger, and Priest

---

* Permanent address: Department of Physics, Mount Carmel College Bangalore, 560 052, India.

(1988) discussed the dynamics of velocity and magnetic fields in coronal loops. Recently Krishan, Sreedharan, and Mahajan (1991) have also presented a Vlasov–Maxwell description of coronal loops which is a preparation for the study of kinetic processes related to heating and acceleration of plasma particles.

The force-free magnetic fields ($\overline{\nabla} \times \overline{B} = \alpha \overline{B}$) and the Beltrami flows ($\overline{\nabla} \times \overline{V} = \alpha \overline{V}$) represent the minimum energy state of a magnetofluid. A single C–K function represents these configurations of the magnetic and velocity fields. The magnetofluid in the coronal loop is believed to be in an approximate state of the force-free fields with small departures from the current-free fields of the photospheric fluid. Now, it is quite reasonable to expect the coronal loop fields and flows to have departures from the strictly force-free configuration. By representing the fields by the superposition of the C–K functions we can manoeuvre these departures in a systematic and quantitative manner.

We extend the earlier work on the steady-state structure of the pressure in coronal loops, by representing the velocity and magnetic fields as the superposition of three Chandrasekar–Kendall functions. This brings in the three-dimensional spatial variation (r, θ, z) in the plasma pressure and the state is not force-free, although individually the C–K functions represent a force-free state. The motivation behind the choice of three (C–K) functions for velocity and magnetic fields is to extend this study to include the time-dependence of pressure in coronal loops. The three-mode representation admits the temporal behavioral of the fields in its most basic form. Besides a three-mode representation also in principle exhibits chaotic behavior. The evolution of the resistive magnetohydrodynamic equillibria is being studied in order to understand the emergence of preferred structures, if any, by Shan, Montgomery, and Chen (1991). A truncated three-mode configuration has been explored by Chen, Shan, and Montgomery (1990) and their results qualitatively agree with the predictions of the minimum dissipation theory (Montgomery, Phillips, and Theobald, 1989) as well as with the computations obtained using the numerical code (Dahlburg *et al.*, 1986, 1987, 1988 and Theobald *et al.*, 1989). We however plan to study the three-mode ideal system in order to qualify the variations of the velocity and magnetic fields in the solar atmosphere, in terms of nonlinear or stochastic fluctuations. In this paper we discuss only the three-dimensional spatial pressure structure of coronal loops.

In the next section, we present the MHD equations for an incompressible fluid and outline the pressure profile. Section 3 deals with a discussion of the results obtained in this study.

2. Derivation of the Pressure Profile

The coronal loop plasma is represented by a cylindrical column of length 'L' and radius 'R'. The mechanical pressure P is expressed as a function of velocity $\overline{V}$ and magnetic field $\overline{B}$ using the MHD equations

$$\frac{\overline{\nabla} P}{\rho} = \frac{(\overline{\nabla} \times \overline{B}) \times \overline{B}}{\rho} - (\overline{V} \cdot \overline{\nabla})\overline{V} - \frac{\partial \overline{V}}{\partial t} , \tag{1a}$$

$$\overline{\nabla} \times (\overline{V} \times \overline{B}) - \frac{\partial \overline{B}}{\partial t} = 0 \,, \tag{1b}$$

where ρ is the mass density and the force due to gravity has been neglected.

Using the identity $(\overline{V} \cdot \overline{\nabla})\overline{V} = (\overline{\nabla} \times \overline{V}) \times \overline{V} + (1/2)\overline{\nabla}V^2$, Equation (1a) becomes

$$\overline{\nabla}[P/\rho + (1/2)V^2] = \left[\frac{(\overline{\nabla} \times \overline{B}) \times \overline{B}}{\rho} - (\overline{\nabla} \times \overline{V}) \times \overline{V} \right] - \frac{\partial \overline{V}}{\partial t} \,. \tag{2}$$

Following Montgomery, Turner, and Vahala (1978), the velocity field $\overline{V}$ and magnetic field $\overline{B}$ in the loop plasma are represented by the superposition of Chandra-sekhar–Kendall functions. The complete dynamics can be described by a set of infinite coupled nonlinear ordinary differential equations which are of first order in time for the expansion coefficients of velocity and magnetic fields and it is a formidable task to find solutions to these equations. Hence, here we choose to represent the fields by the superposition of the three lowest order C–K functions. Another justification for doing so is that these functions represent the largest spatial scales and therefore may be the most suitable states for comparison with observed phenomena.
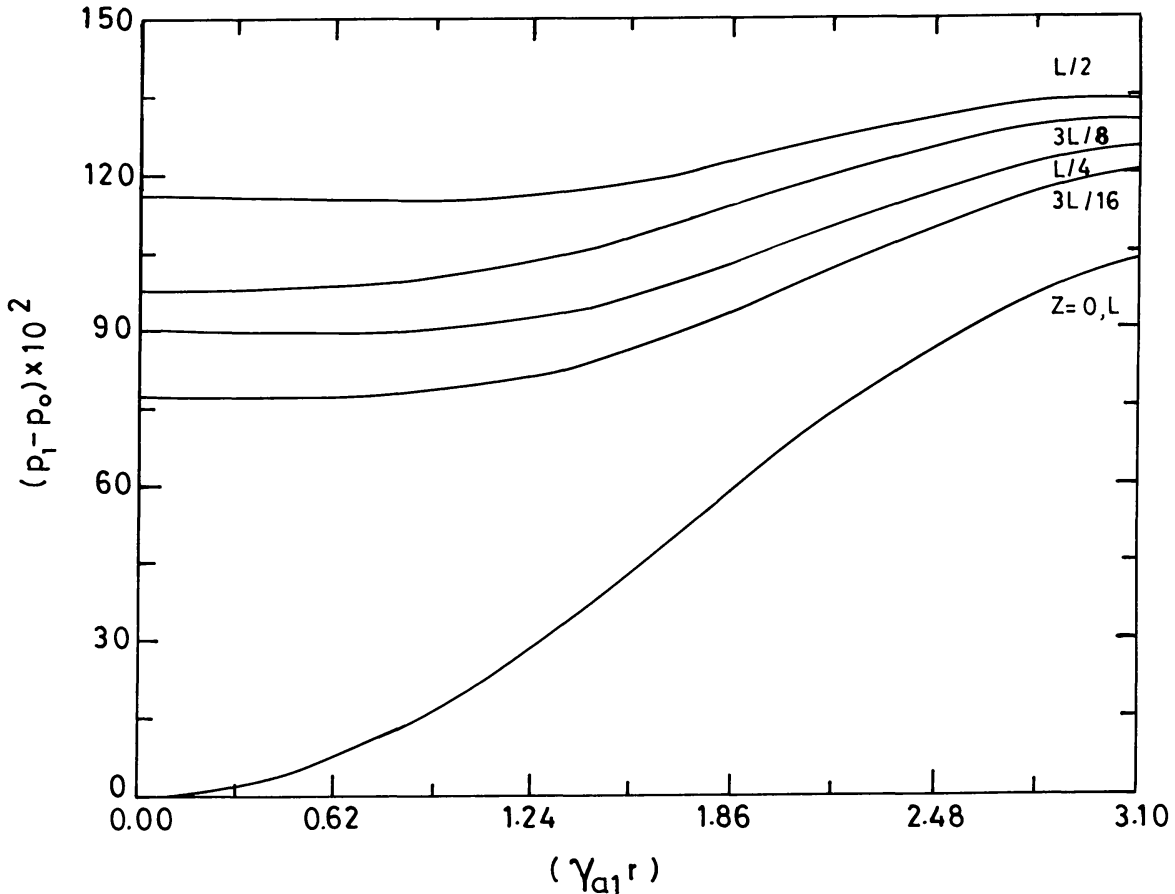

Fig. 1.   Radial variation of the pressure P_1 for different axial distances, Z.

In the triple-mode system,

$$\overline{V} = \lambda_a \eta_a(t)\overline{A}_a + \lambda_b \eta_b(t)\overline{A}_b + \lambda_c \eta_c(t)\overline{A}_c, \tag{3}$$

$$\overline{B} = \lambda_a \xi_a(t)\overline{A}_a + \lambda_b \xi_b(t)\overline{A}_b + \lambda_c \xi_c(t)\overline{A}_c, \tag{4}$$

$$\overline{a}_{nm}(r) = \hat{e}_r \left[\frac{im}{r} + \frac{ik_n}{\lambda_{nm}} \frac{\partial}{\partial r} \right] \psi_{nm} + \hat{e}_\theta \left[-\frac{\partial}{\partial r} - \frac{mk_n}{r\lambda_{nm}} \right] \psi_{nm} +$$

$$+ \hat{e}_z \left[\frac{\lambda_{nm}^2 - k_n^2}{\lambda_{nm}} \right] \psi_{nm}, \tag{5}$$

where

$$\psi_{nm} = J_m(\gamma_{nm}r) \exp(im\theta + ik_n z),$$

$$\lambda_{nm} = \mp (\gamma_{nm}^2 + k_n^2)^{1/2}, \qquad k_n = 2\pi n/L, \quad \begin{array}{l} n = 0, \mp 1, \mp 2, \ldots, \\ m = 0, \mp 1, \mp 2, \ldots, \end{array}$$

$$\overline{A}_{nm} = C_{nm}\overline{a}_{nm}(r);$$

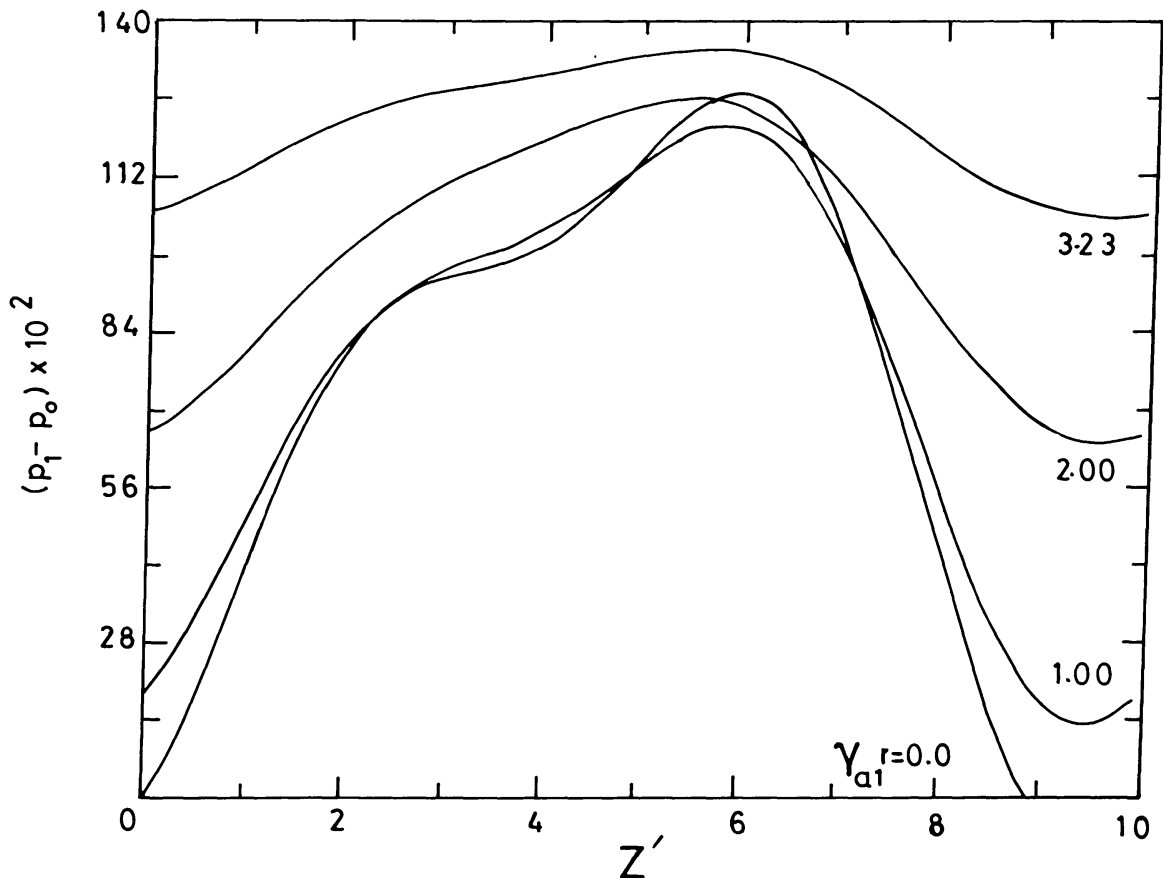η's and ξ's are in general complex.

Fig. 2.   Axial variation of the pressure P_1 for different radial distances, r.
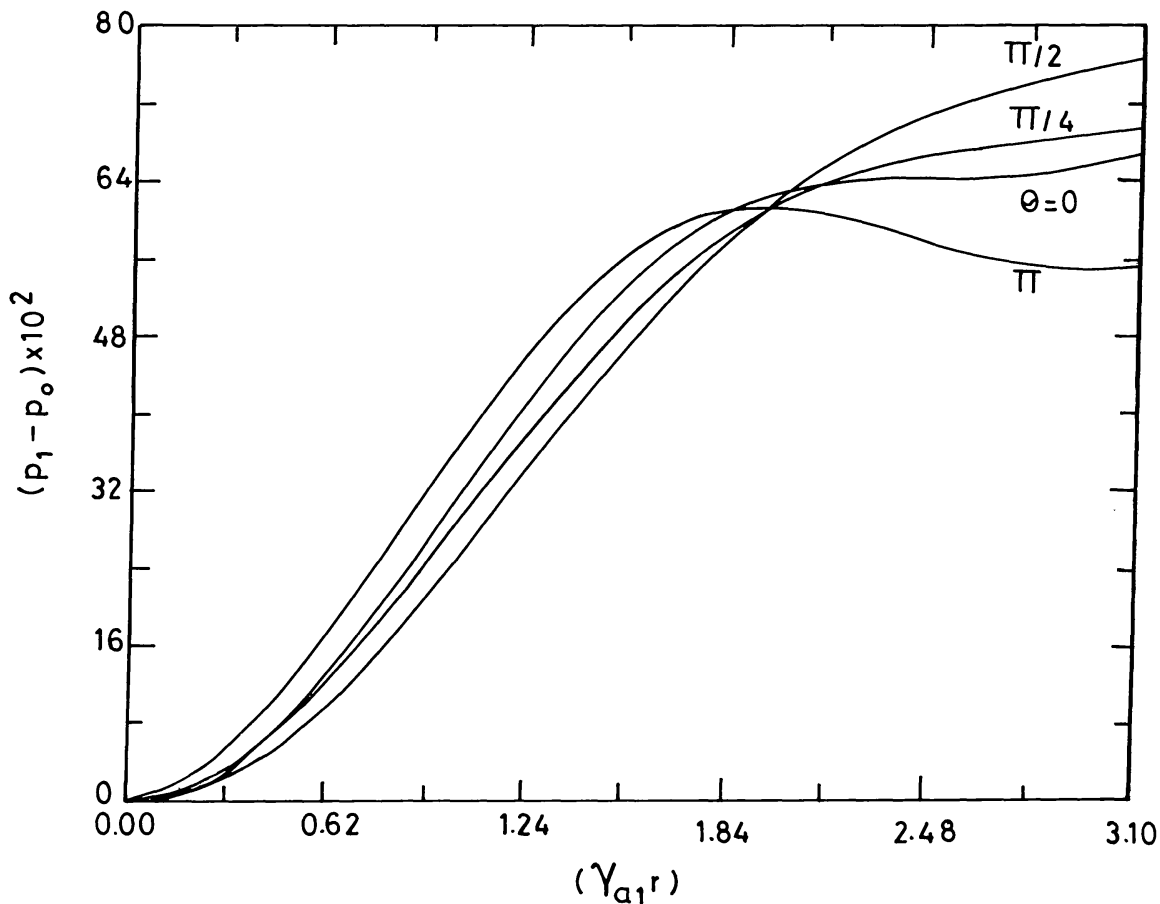
Fig. 3.   Radial variation of the pressure P_1 for different azimuthal angles, θ.
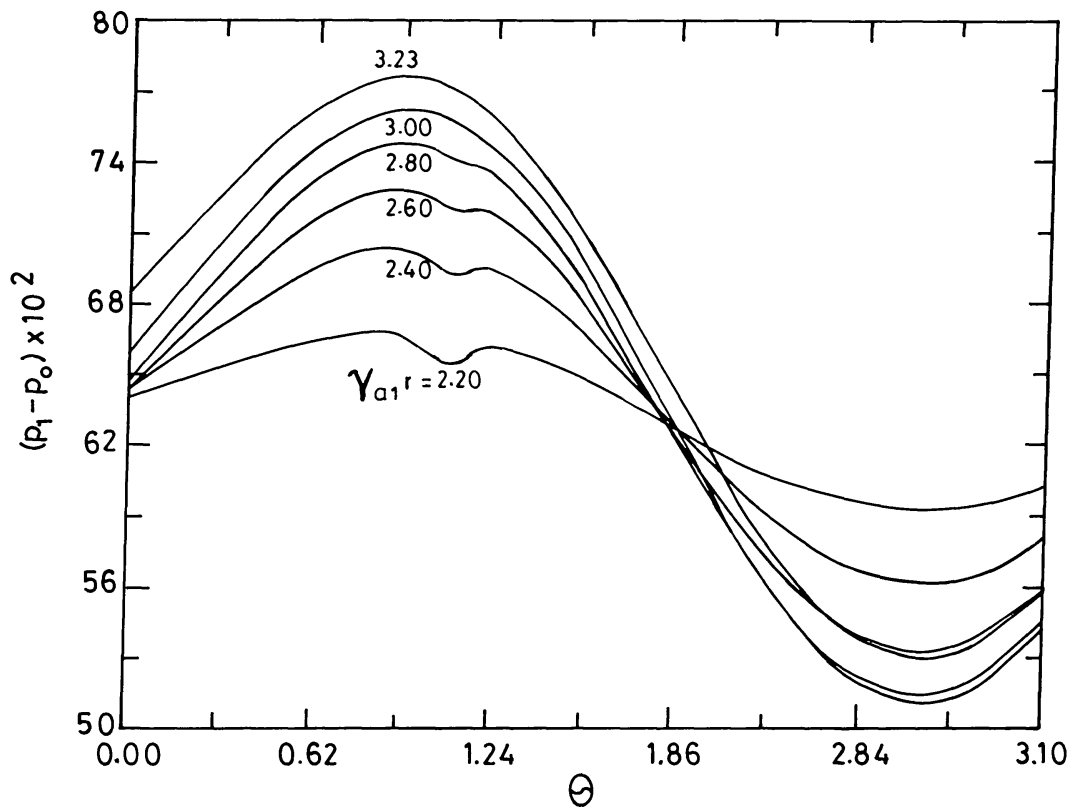
Fig. 4.   Azimuthal variation of the pressure P_1 for $\gamma_{a1}r$ = 2.2 to 3.23.

The functions $\bar{a}_{nm}$ satisfy $\bar{\nabla} \times \bar{a}_{nm} = \lambda_{nm}\bar{a}_{nm}$. γ_{nm} can be determined from the boundary conditions for a perfectly conducting and rigid boundary since the observations do show very well-defined loop structures aligned with the magnetic field across which there is little or no transport. Thus the radial component of the velocity and the magnetic field vanish at the surface $r = R$, i.e.,

$$R k_n \gamma_{nm} J'_m(\gamma_{nm}R) + m\lambda_{nm} J_m(\gamma_{nm}R) = 0 \ . \tag{6}$$

However, for the $(n = 0 = m)$ mode, $V_r = B_r = 0$, and the γ_{00} is determined from the constancy of the ratio of the toroidal and poloidal magnetic fluxes as

$$\frac{\psi_t}{\psi_p} = -\frac{J'_0(\gamma_{00}R)}{J_0(\gamma_{00}R)}\frac{R}{L}\frac{\gamma_{00}}{\lambda_{00}} \ ; \tag{7}$$
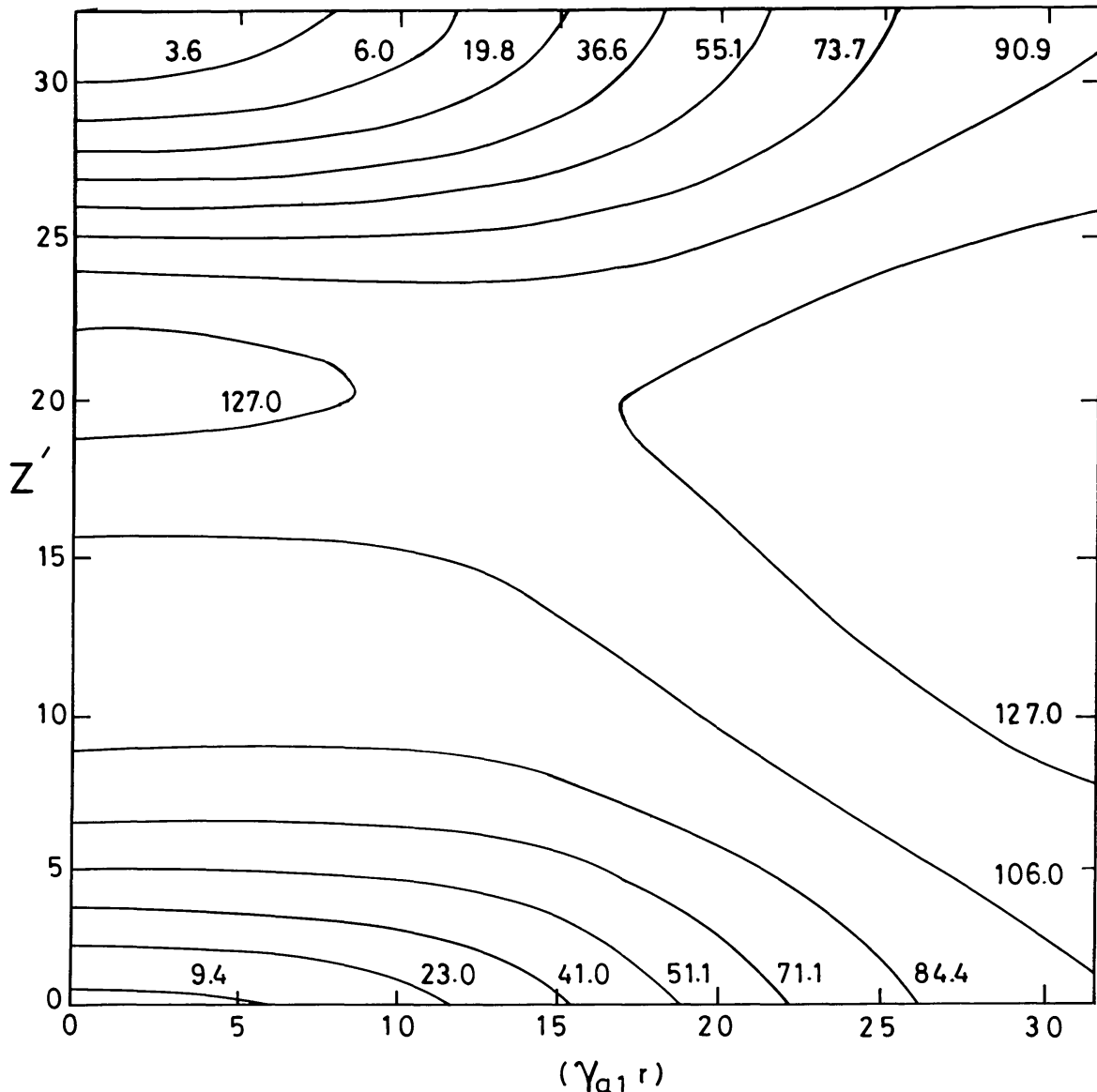

Fig. 5.   Contour plot of the pressure P_1 as a function of $\gamma_{a1}r$ and Z' when θ is averaged. Each unit of the axes corresponds to $\gamma_{a1}r = 0.1$ and $Z' = 0.3$, respectively.

C_{nm} is the normalizing constant which relates $\overline{A}_{nm}$ to $\overline{a}_{nm}$ by

$$\overline{A}_{nm} = C_{nm}\overline{a}_{nm} \quad \text{and} \quad \int \overline{A}^*_{n'm'} \cdot \overline{A}_{nm} \, \mathrm{d}^3r = \delta_{nn'}\delta_{mm'} \ .$$

The dynamics can be described by taking the inner products of the curl of Equations (1a) and (1b) with A^*_{nm} and integrating over the volume. The resulting six complex, coupled nonlinear ordinary differential equations are

$$\frac{\partial \eta_a}{\partial t} = \frac{\lambda_b \lambda_c}{\lambda_a}(\lambda_c - \lambda_b)I[\eta_b \eta_c - \xi_b \xi_c/\rho] \, , \tag{8}$$

$$\frac{\partial \eta_b}{\partial t} = \frac{\lambda_c \lambda_a}{\lambda_b}(\lambda_a - \lambda_c)I^*[\eta_c^* \eta_a - \xi_c^* \xi_a/\rho] \, , \tag{9}$$

$$\frac{\partial \eta_c}{\partial t} = \frac{\lambda_a \lambda_b}{\lambda_c}(\lambda_b - \lambda_a)I^*[\eta_a \eta_b^* - \xi_b^* \xi_a/\rho] \, , \tag{10}$$
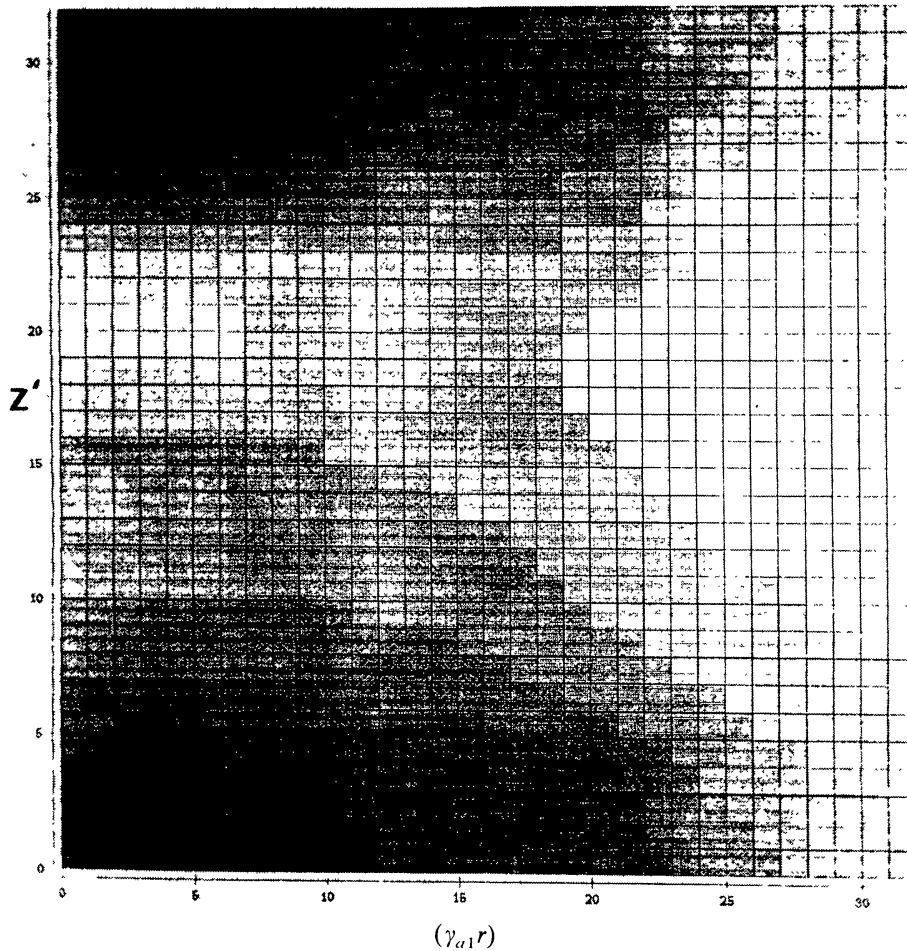

Fig. 6a. Density plot of the pressure P_1 as a function of $\gamma_{a1}r$ and Z'.
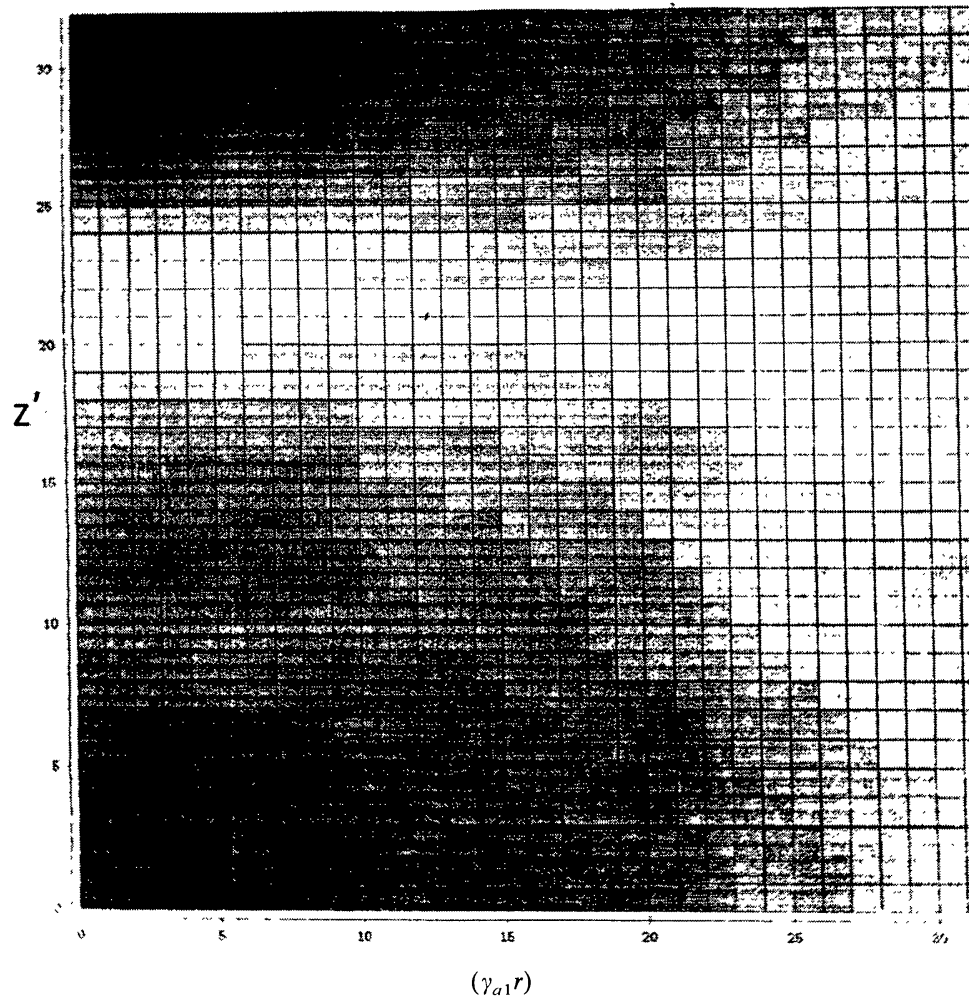
$$(\gamma_{a1}r)$$

Fig. 6b.   Same as in Figure 6(a) for $\eta_{b1} > \eta_{c1}$.

$$\frac{\partial \xi_a}{\partial t} = \lambda_b \lambda_c I \left[\eta_b \xi_c - \eta_c \xi_b \right], \tag{11}$$

$$\frac{\partial \xi_b}{\partial t} = \lambda_c \lambda_a I^* \left[\eta_c^* \xi_a - \eta_a \xi_c^* \right], \tag{12}$$

$$\frac{\partial \xi_c}{\partial t} = \lambda_a \lambda_b I^* \left[\eta_a \xi_b^* - \eta_b^* \xi_a \right], \tag{13}$$

where $I = \int \overline{A}_a^* \cdot (\overline{A}_b \times \overline{A}_c) \, \mathrm{d}^3 r$ and the (n, m) values of the modes (a, b, c) satisfy the conditions $n_a = n_b + n_c$ and $m_a = m_b + m_c$.
It can be shown that

$$(\overline{\nabla} \times \overline{B}) \times \overline{B} = \sum_{\substack{i = a,\, b,\, c \\ j = b,\, c,\, a}} \lambda_i \lambda_j \xi_i \xi_j (\lambda_i - \lambda_j) \overline{A}_i \times \overline{A}_j, \tag{14}$$

$$(\overline{\nabla} \times \overline{V}) \times \overline{V} = \sum_{\substack{i = a,\, b,\, c \\ j = b,\, c,\, a}} \lambda_i \lambda_j \eta_i \eta_j (\lambda_i - \lambda_j) \overline{A}_i \times \overline{A}_j \,, \tag{15}$$

so that

$$\overline{\nabla}(P/\rho + (1/2)V^2) = \sum_{\substack{i = a,\, b,\, c \\ j = b,\, c,\, a}} \lambda_i \lambda_j (\lambda_i - \lambda_j) \left(\frac{\xi_i \xi_j}{\rho} - \eta_i \eta_j \right) \overline{A}_i \times \overline{A}_j - \frac{\partial \overline{V}}{\partial t} \,. \tag{16}$$

In this paper we confine our study to the steady-state solution to the pressure. For the steady-state $\partial/\partial t\ [\eta, \xi] = 0$, and hence, we find from Equations (8) to (13)

$$\eta_a = \xi_a/\rho^{1/2}, \quad \eta_b = \xi_b/\rho^{1/2} \quad \text{and} \quad \eta_c = \xi_c/\rho^{1/2} \,.$$

Equation (16) reduces to

$$\nabla(P/\rho + (1/2)V^2) = 0 \,,$$

i.e., $P/\rho + 1/2V^2 = $ constant.

If the value of P at the origin ($r = 0$, $z = 0$) is P_0, then

$$P/\rho = P_0/\rho + (1/2)V_0^2 - (1/2)V^2 \,, \tag{17}$$

where V_0 is the velocity at the origin ($r = 0$, $z = 0$).

3. Discussion

The spatial variation of pressure is presented for a cylindrical column of plasma for which the ratio of the radius R to length L has been taken to be $R/L = \frac{1}{10}$ and the ratio of the toroidal to poloidal flux $\psi_t/\psi_p = 0.1$.

We have chosen two triads a, b, c such that they represent the largest possible spatial scales, as well as satisfy the condition $a = b + c$. These are:

$$a_1 = (1, 1), \quad b_1 = (1, 0), \quad \text{and} \quad c_1 = (0, 1);$$
$$a_2 = (0, 0), \quad b_2 = (1, 1), \quad \text{and} \quad c_2 = (-1, -1).$$

The corresponding values of γ's and λ's are found to be (from Equations (6) and (7))

$$\gamma_{a1} R = 3.23, \quad \gamma_{b1} R = 3.85, \quad \gamma_{c1} R = 3.85 \,,$$
$$\lambda_{a1} R = 3.29, \quad \lambda_{b1} R = 3.90, \quad \lambda_{c1} R = 3.85 \,,$$

and

$$\gamma_{a2} R = 1.44, \quad \gamma_{b2} R = 3.23, \quad \gamma_{c2} R = 3.23 \,,$$
$$\lambda_{a2} R = 1.44, \quad \lambda_{b2} R = 3.29, \quad \lambda_{c2} R = 3.29 \,.$$

The total energy E of the loop plasma in a given configuration (a, b, c) is given by $E = 2 \Sigma_{i = a,\, b,\, c}\, \lambda_i^2 \eta_i^2$. Though we have some estimate of the total energy of a typical loop there is no obvious way of fixing the relative magnitudes of the three modes. However, there are two physical considerations we can use to fix the relative strengths of the three modes, as is usually done whenever three mode interactions are involved.
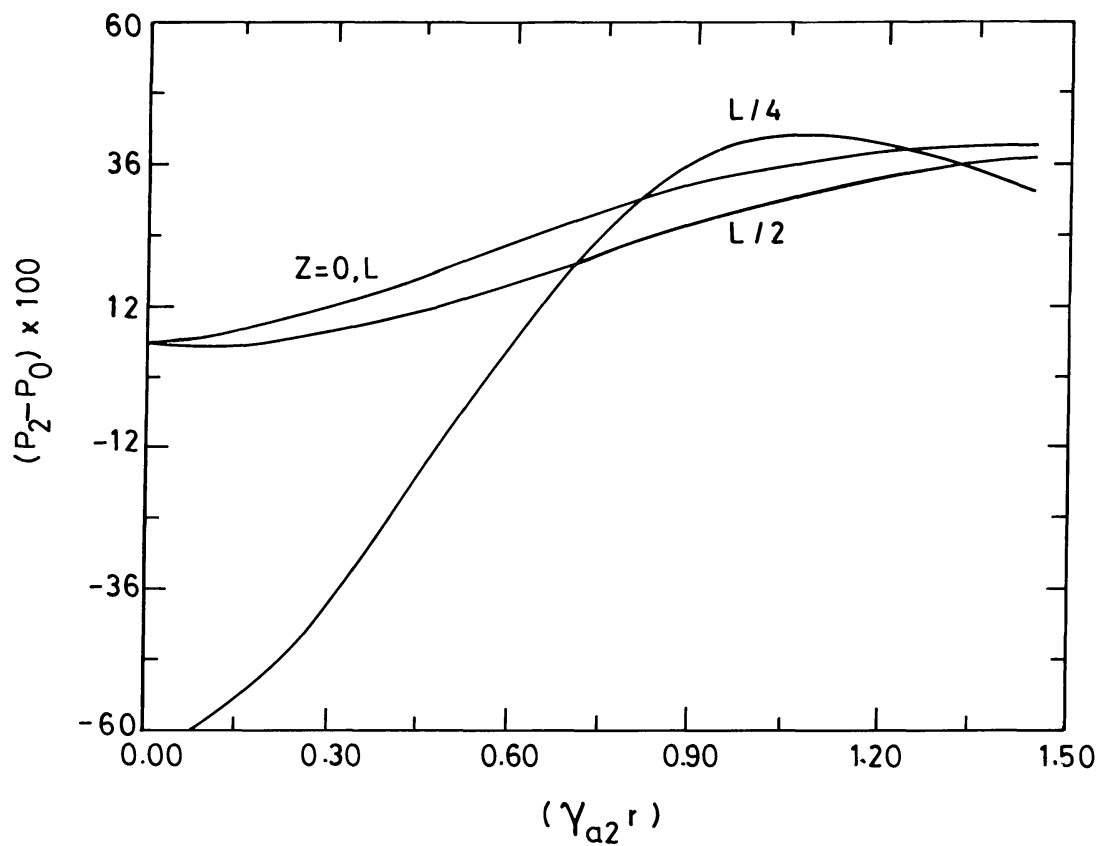
Fig. 7a.   Radial variation of the pressure P_2 for $\theta = \pi/4$ and different axial distances.
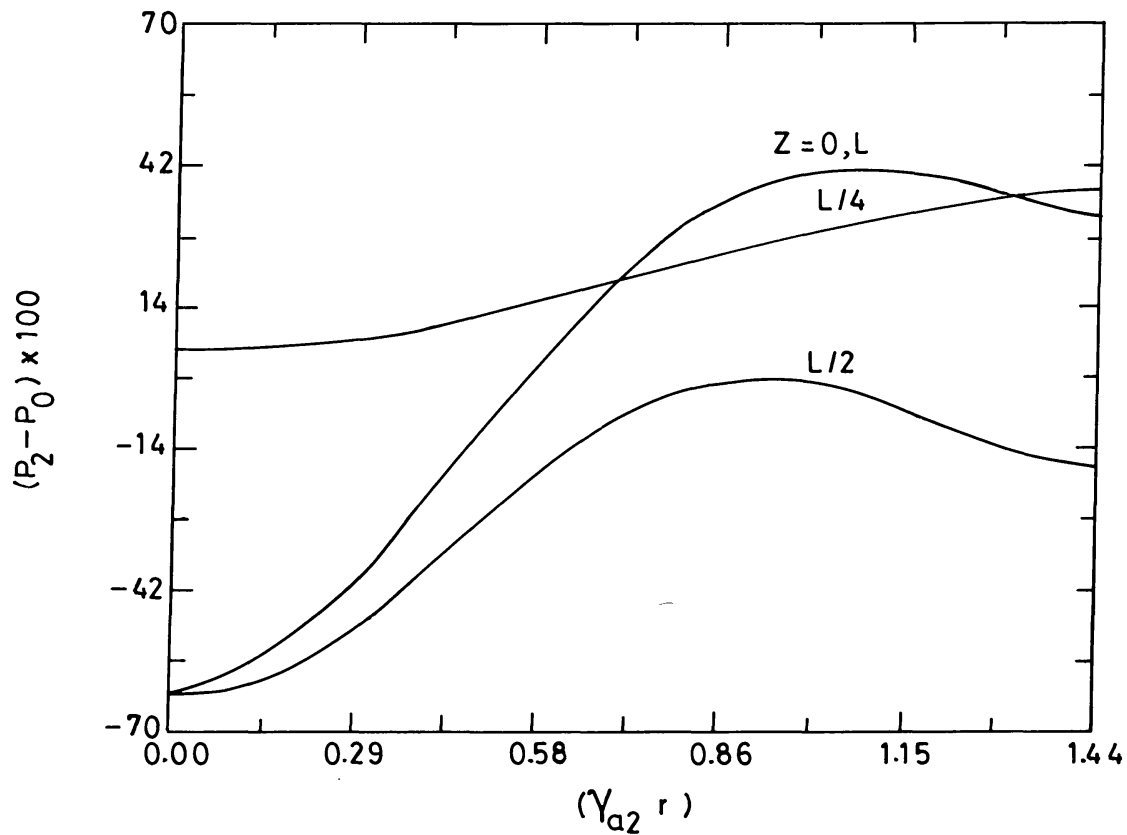

Fig. 7b.   Radial variation of the pressure P_2 for $\theta = 3\pi/4$ and different axial distances.

3.1. CASE I

The first is the pump approximation under which one of the three modes is taken to be the strongest. For example, here since the conservation conditions give a = b + c, we can take 'a' to be the dominant mode and call it the pump which shares its energy with the other two modes. This will become evident in the time-dependent description. Therefore, let

$$\lambda_a^2 \eta_a^2 > \lambda_b^2 \eta_b^2 \quad \text{and} \quad \lambda_a^2 \eta_a^2 > \lambda_c^2 \eta_c^2 . \tag{18}$$

3.1.1. *Pressure* (P_1) *Structure in the Configuration* (a_1, b_1, c_1)

For the triad (a_1, b_1, c_1)

$$\eta_{b1}/\eta_{a1} < \lambda_{a1}/\lambda_{b1} = 0.8435 \quad \text{and} \quad \eta_{c1}/\eta_{a1} < \lambda_{a1}/\lambda_{c1} = 0.8658.$$

We choose

$$|\eta_{a1}| = 10^7, \qquad |\eta_{b1}| = 8 \times 10^6 = |\eta_{c1}| ,$$

so that the pump approximation is valid. The expression on the right-hand side of Equation (17) has been averaged over a full cycle of θ and pressure $(P_1 - P_0)$ is plotted as a function of $\gamma_{a1}r$ for different values of z' ($z' = (z/L) \times 10$) in Figure 1. It can be seen that the pressure (or temperature) at any height increases along the radius towards the surface. The radial variation of pressure is the maximum at the foot points of the loop and it is minimum at the apex. This is in confirmation with the result of Levine and Withbroe (1977) who showed that the coronal loops undergoing dynamic changes are
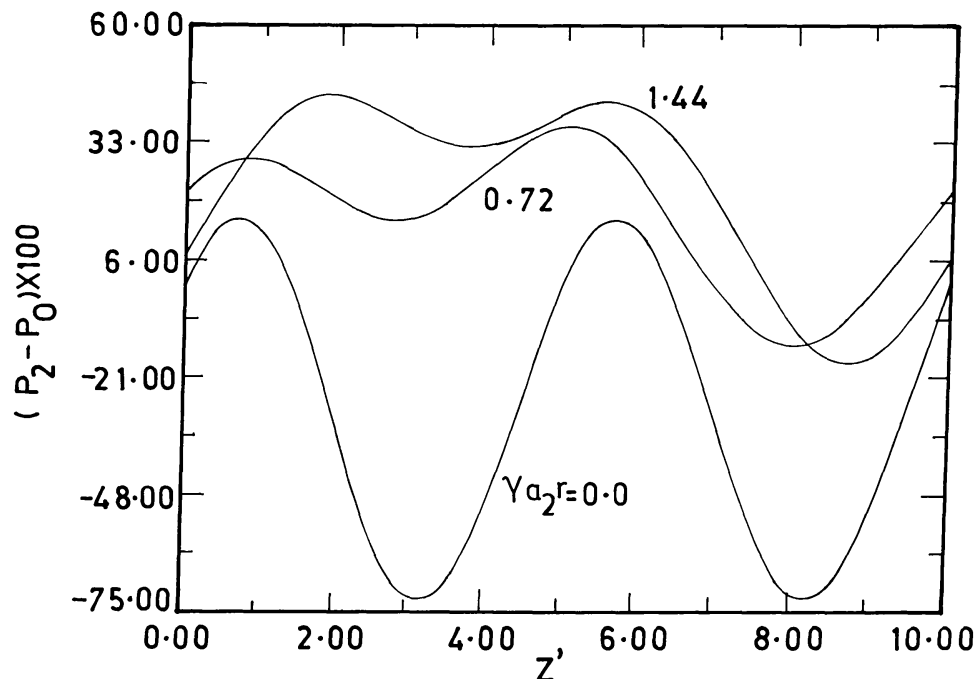

Fig. 8. Axial variation of the pressure P_2 for $\theta = \pi/4$ and different radial distances.

characterized by a temperature structure in which there is a cool core relative to the substantially hot surrounding sheath.

In Figure 2, $(P_1 - P_0)$ is plotted against z' for various values of $(\gamma_{a1}r)$. The axial variation of the pressure is maximum at the axis and minimum at the surface. The maximum value of the pressure is attained near the apex for all values of $(\gamma_{a1}r)$. This is in agreement with the results of Rosner, Tucker, and Vaiana (1978).

Figure 3 presents the radial variation of the pressure for $\theta = 0$, $\pi/4$, $\pi/2$, and π when the pressure is averaged over z. The pressure increases uniformly for all values of $\gamma_{a1}r \leq 2.0$. However, for $\gamma_{a1}r > 2$ the dependence of the pressure on the azimuthal angle is significant.

Figure 4 shows the azimuthal variation of the pressure for different values of $\gamma_{a1}r > 2.0$. The pressure exhibits an oscillatory behavior predominantly near the surface.

Figure 5 depicts the contour plot of pressure as functions of $\gamma_{a1}r$ and z' when the pressure is averaged over θ.

Figure 6(a) is the density plot of the pressure. The darkest region corresponds to the minimum pressure. As we proceed towards the apex, the shades become lighter and the region of maximum pressure is reached. Figure 6(b) is the density plot of the pressure when $\eta_{b1} > \eta_{c1}$. It is seen that the region of the maximum pressure has moved up. However, when $\eta_{c1} > \eta_{b1}$, the region of the maximum pressure has shifted down. Thus the region of maximum pressure need not necessarily be at the apex.
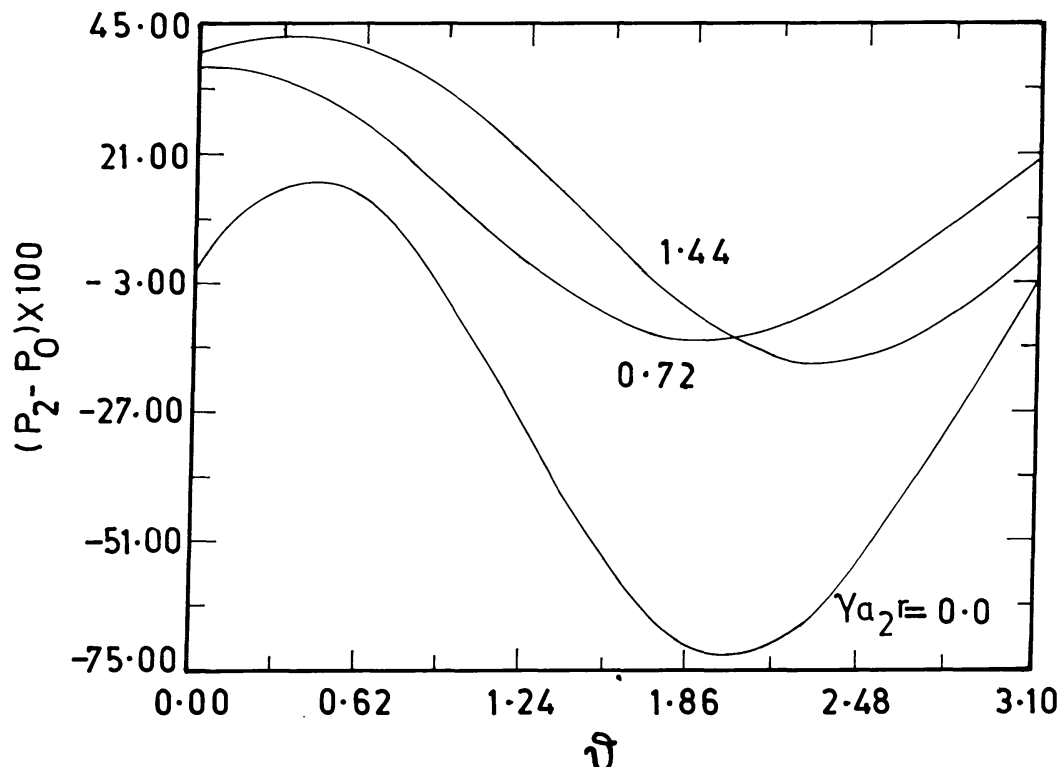

Fig. 9.   Azimuthal variation of the pressure P_2 for $Z = L/2$ and different radial distances.

3.1.2. *Pressure (P_2) Structure in the Configuration (a_2, b_2, c_2)*

For the triad $a_2 \equiv (0, 0)$, $b_2 \equiv (1, 1)$, $c_2 \equiv (-1, -1)$, using the inequality (18) and the values $|\eta_{a2}| = 2 \times 10^7$, $|\eta_{b2}| = 8 \times 10^6 = |\eta_{c2}|$, we arrive at the following results:

Figure 7(a) presents the radial variation of the pressure for $\theta = \pi/4$ and for different axial positions. In this case the maximum pressure as well as the maximum variation in pressure is found at $z = L/4$.

Figure 7(b) shows the radial variation of pressure for $\theta = 3\pi/4$ and for $z = 0, L/4, L/2$, and L. Here, the maximum pressure as well as the maximum variation in pressure is at the foot points, in contrast to the case for $\theta = \pi/4$.

The axial variation of pressure for $\theta = \pi/4$ and $\gamma_{a2}r = 0, 0.72$, and 1.44 is given in Figure (8). The pressure shows an oscillatory behavior at the axis of the loop more predominantly than towards the surface.

Figure 9 depicts the azimuthal variation of the pressure at the apex of the loop for different radial distance from the axis. In this case also the oscillatory nature of pressure is evident. The maximum value is attained at the boundary.

3.2. CASE II

3.2.1. *Pressure (P_1) Structure in the Configuration (a_1, b_1, c_1)*

The second physical consideration that can guide us is that the mode strengths vary in proportion to their spatial scales. The mode with the largest spatial scale may be the
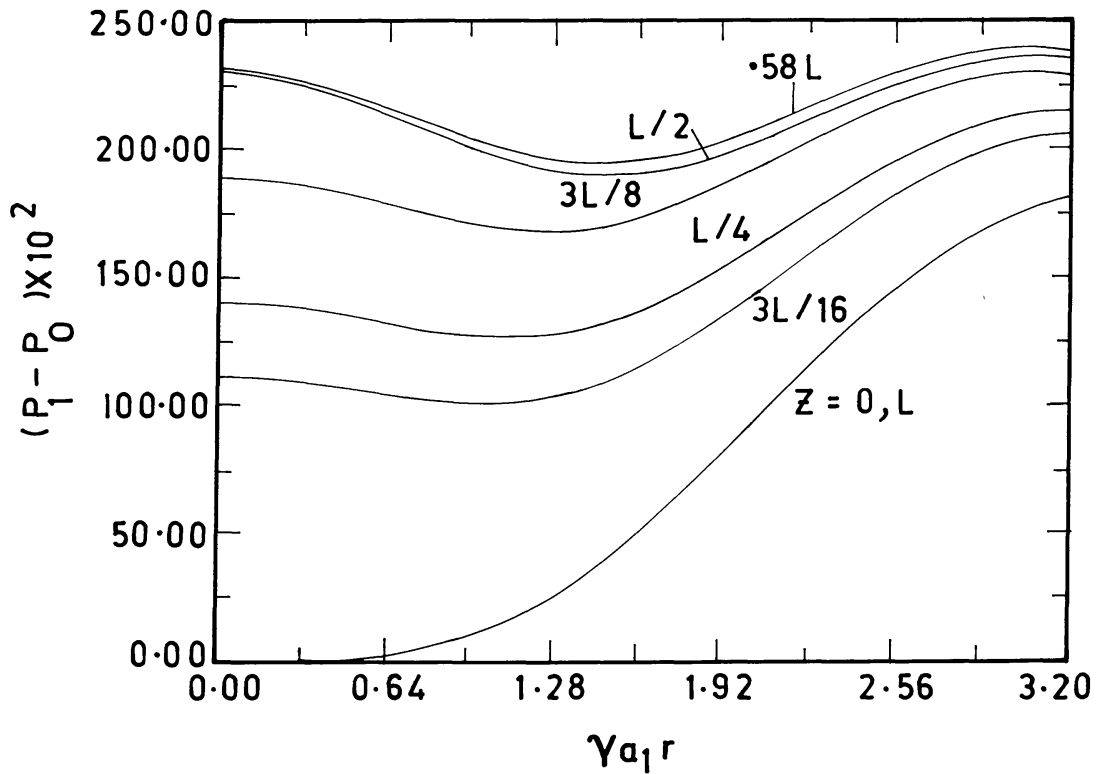

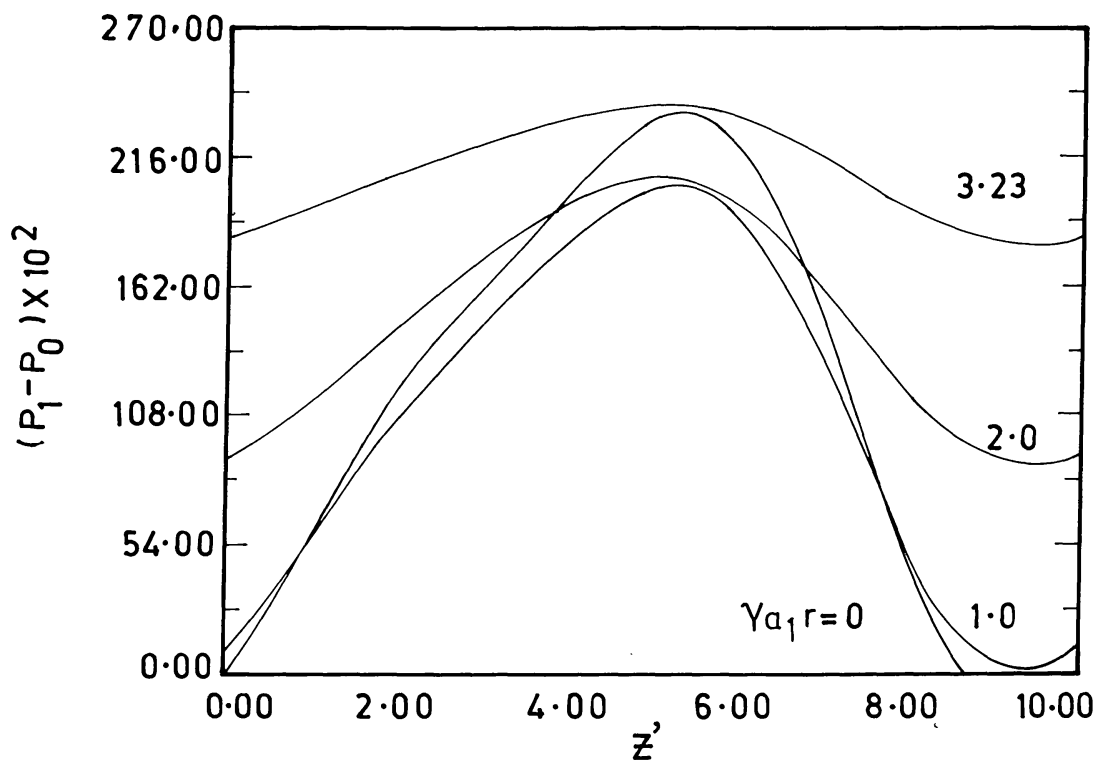Fig. 10.   Same as in Figure 1 for $\eta_{c1} > \eta_{a1}$.

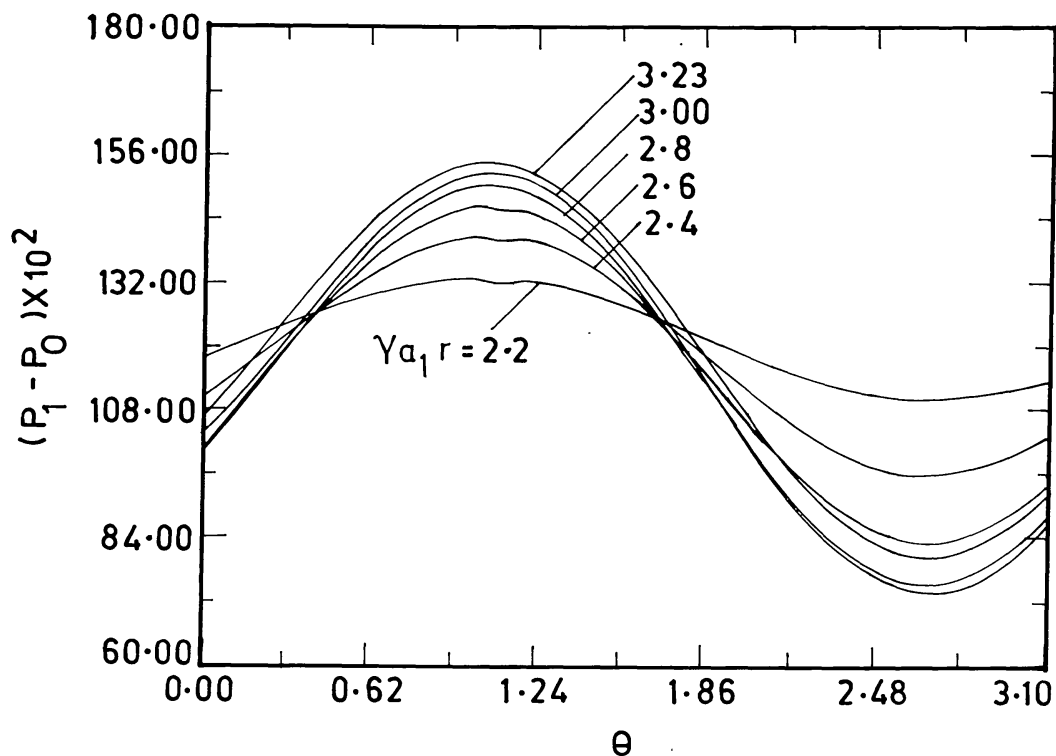Fig. 11.   Same as in Figure 2 for $\eta_{c1} > \eta_{a1}$.

Fig. 12.   Same as in Figure 4 for $\eta_{c1} > \eta_{a1}$.

strongest. Here since $a_1 \equiv (1, 1)$ and $b_1 \equiv (1, 0)$ have the same spatial scale in the z'-direction and this spatial scale is smaller than that of the mode $c_1 \equiv (0, 1)$, we can assume 'a_1' and 'b_1' to be of equal strength and less than the strength of 'c_1', i.e.,

$$\lambda_{a1}^2 \eta_{a1}^2 = \lambda_{b1}^2 \eta_{b1}^2, \quad \lambda_{a1}^2 \eta_{a1}^2 < \lambda_{c1}^2 \eta_{c1}^2;$$

we chose $|\eta_{a1}| = 10^7$, $|\eta_{b1}| = 8.4 \times 10^6$, and $|\eta_{c1}| = 1.6 \times 10^7$ so that the above conditions are satisfied. The radial pressure variation is presented in Figure 10 for different axial positions. The maximum variation of the pressure is at the foot points as in Figure 1. However, for other values of Z', the pressure tends to decrease initially and then increases monotonically after a certain radial distance, contrary to the pressure profile given in Figure 1, where one sees a monotonically increasing pressure for all values of Z'.

The axial and azimuthal variations of the pressure are given in Figures 11 and 12, respectively. The trend is very similar to that presented in Figures 2 and 3.

3.2.2. *Pressure* (P_2) *Structure in the Configuration* (a_2, b_2, c_2)

In this case the mode $a_2 \equiv (0, 0)$ corresponds to the largest spatial scale and therefore if this is stronger than the other two we arrive at the conditions $\lambda_{a2}^2 \eta_{a2}^2 > \lambda_{b2}^2 \eta_{b2}^2$ and $\lambda_{a2}^2 \eta_{a2}^2 > \lambda_{c2}^2 \eta_{c2}^2$ which are identical to the pump case for the triad (a_2, b_2, c_2) and the pressure profiles have already been discussed.

3.3 CONCLUSION

In conclusion, the representation of velocity and magnetic fields by a three-mode Chandrasekhar–Kendall functions brings out the three-dimensional features of the pressure profile. We believe that the choice of the triads representing the variations of velocity and magnetic fields on the largest spatial scales permitted by the system, provides a fairly realistic description of the loop plasma. Though the pressure structure is a strong function of the relative amplitudes of the modes, the trends, like an increase of pressure towards the surface and the existence of maximum somewhere along the length of the loop, emerge as the general features. The temporal evolution of the pressure is being considered and will be reported shortly.

References

Aschwanden, M. J.: 1987, *Solar Phys.*, **111**, 113.
Chen, H., Shan, X., and Montgomery, D.: 1990, *Phys. Rev.* **A42**, 6158.
Dahlburg, J. P., Montgomery, D., Doolen, G. D., and Turner, L.: 1986, *Phys. Rev. Letters* **57**, 428.
Dahlburg, J. P., Montgomery, D., Doolen, G. D., and Turner, L.: 1987, *J. Plasma Phys.* **37**, 299.
Dahlburg, J. P., Montgomery, D., Doolen, G. D., and Turner, L.: 1988, *J. Plasma Phys.* **40**, 39.
Foukal, P. V.: 1978, *Astrophys. J.* **223**, 1046.
Hood, A. W. and Priest, E. R.: 1979, *Astron. Astrophys.* **77**, 233.
Krieger, A. S., de Feiter, L.D., and Vaiana, G. S.: 1976, *Solar Phys.* **47**, 117.
Krishan, V.: 1983a, in *Proceedings of the Spring College on Radiation in Plasmas*, Trieste, Italy.
Krishan, V.: 1983b, *Solar Phys.* **88**, 155.
Krishan, V.: 1985, *Solar Phys.* **95**, 269.

Krishan, V., Berger, M. and Priest, E. R.: 1988, in R. C. Altrock (eds.), *Solar and Stellar Coronal Structures and Dynamics*, National Solar Observatory.

Krishan, V., Sreedharan, T. D., and Mahajan, S. M.: 1991, *Monthly Notices Roy. Astron. Soc.* **249**, 596.

Levine, R. H. and Altschuler, M. D.: 1974, *Solar Phys.* **36**, 345.

Levine, R. H. and Withbroe, G. L.: 1977, *Solar Phys.* **51**, 83.

Montgomery, D., Philips, L., and Theobald, M. L.: 1989, *Phys. Rev.* **A40**, 1515.

Montgomery, D., Turner, L. and Vahala, G.: 1978, *Phys. Fluids* **21**, 757.

Poletto, G., Vaiana, G. S., Zomback, M.V. Krieger, A. S., and Timothy, A. F.: 1975, *Solar Phys.* **44**, 83.

Priest, E. R.: 1978, Solar Phys. 58, 57.

Priest, E. R.: 1981, in E. R. Priest (ed.), *Solar Flare Magnetohydrodynamics*, Gordon and Breach, New York, pp. 2 and 139.

Rosner, R., Tucker, W. H. and Vaiana, G. S.: 1978. *Astrophys. J.* **220**, 643.

Shan, X., Montgomery, D., and Chen, H.: 1991, *Phys. Rev.* **A44**, No. 10, 6800.

Theobald, M. L., Montgomery, D., Doolen, G.D., and Dahlburg, J. P.: 1989, *Phys. Fluids*. **B1**, 766.

Tsinganos, K. C.: 1982, *Astrophys. J.* **259**, 820.

Vaiana, G. S. and Rosner, R.: 1978, *Ann. Rev. Astrophys.* **16**, 393.

Yoshida, Z. and Giga, Y. M.: 1990, *Math. Z*. **204**, 235.